

Appendix D

Latest Quaternary paleoseismology and evidence of distributed dextral shear along the
Mohawk Valley fault zone, northern Walker Lane, California

Ryan D. Gold, Richard W. Briggs, Stephen F. Personius, Anthony J. Crone,
Shannon A. Mahan, and Stephen J. Angster

RESEARCH ARTICLE

10.1002/2014JB010987

Key Points:

- Paleoseismic trench investigation along Mohawk Valley fault zone, California
- Four prehistoric earthquakes since 14 ka
- Northern Walker Lane characterized by distributed deformation

Supporting Information:

- Readme
- Figure S1
- Figure S2
- Figure S3
- Figure S4
- Figure S5
- Figure S6
- Figure S7
- Table S1
- Text S1

Correspondence to:

R. D. Gold,
rgold@usgs.gov

Citation:

Gold, R. D., R. W. Briggs, S. F. Personius, A. J. Crone, S. A. Mahan, and S. J. Angster (2014), Latest Quaternary paleoseismology and evidence of distributed dextral shear along the Mohawk Valley fault zone, northern Walker Lane, California, *J. Geophys. Res. Solid Earth*, 119, 5014–5032, doi:10.1002/2014JB010987.

Received 27 JAN 2014

Accepted 29 MAR 2014

Accepted article online 3 APR 2014

Published online 2 JUN 2014

Latest Quaternary paleoseismology and evidence of distributed dextral shear along the Mohawk Valley fault zone, northern Walker Lane, California

Ryan D. Gold¹, Richard W. Briggs¹, Stephen F. Personius¹, Anthony J. Crone¹, Shannon A. Mahan², and Stephen J. Angster^{1,3}

¹Geologic Hazards Science Center, U.S. Geological Survey, Denver, Colorado, USA, ²Crustal Geophysics and Geochemistry Science Center, U.S. Geological Survey, Denver, Colorado, USA, ³Now at Department of Geological Sciences and Engineering, University of Nevada, Reno, Nevada, USA

Abstract The dextral-slip Mohawk Valley fault zone (MVFZ) strikes northwestward along the eastern margin of the Sierra Nevada in the northern Walker Lane. Geodetic block modeling indicates that the MVFZ may accommodate ~3 mm/yr of regional dextral strain, implying that it is the highest slip-rate strike-slip fault in the region; however, only limited geologic data are available to constrain the system's slip rate and earthquake history. We mapped the MVFZ using airborne lidar data and field observations and identified a site near Sulphur Creek for paleoseismic investigation. At this site, oblique dextral-normal faulting on the steep valley margin has created a closed depression that floods annually during spring snowmelt to form an ephemeral pond. We excavated three fault-perpendicular trenches at the site and exposed pond sediment that interfingers with multiple colluvial packages eroded from the scarp that bounds the eastern side of the pond. We documented evidence for four surface-rupturing earthquakes on this strand of the MVFZ. OxCal modeling of radiocarbon and luminescence ages indicates that these earthquakes occurred at 14.0 ka, 12.8 ka, 5.7 ka, and 1.9 ka. The mean ~4 kyr recurrence interval is inconsistent with slip rates of ~3 mm/yr; these rates imply surface ruptures of more than 10 m per event, which is geologically implausible for the subdued geomorphic expression and 60 km length of the MVFZ. We propose that unidentified structures not yet incorporated into geodetic models may accommodate significant dextral shear across the northern Walker Lane, highlighting the role of distributed deformation in this region.

1. Introduction

A basic issue in active tectonic studies is explaining discrepancies between strain measurements across active faults that sample deformation at different timescales [e.g., Bennett *et al.*, 2004; Cowgill *et al.*, 2009; Friedrich *et al.*, 2003]. At the annual to decadal timescales, geodetic measurements from GPS and interferometric synthetic aperture radar can provide nearly complete spatial coverage of elastic strain accumulation across regions of active deformation [e.g., Elliott *et al.*, 2008; Elliott *et al.*, 2012; Fialko, 2006; McClusky *et al.*, 2001]; however, these methods sample a short temporal record of regional strain that can be sensitive to transient interseismic strain [e.g., Amos *et al.*, 2013] and cannot uniquely resolve strain accumulation on individual faults with overlapping elastic deformation fields [e.g., Dixon *et al.*, 1995]. In contrast, geologic slip-rate studies of faulted and dated landforms, such as fluvial terraces, alluvial fans, and glacial moraines, define a cumulative record of elastic strain energy release that spans thousands of years [Matmon *et al.*, 2006; Sieh and Jahns, 1984; Van der Woerd *et al.*, 1998]; however, these studies are limited in their spatial coverage and vulnerable to incomplete documentation of off-fault deformation [Bird, 2009; Shelef and Oskin, 2010]. Resolving and understanding the sources of discrepancies that arise from these different methodologies is critical for seismic hazard analysis [Petersen *et al.*, 2008].

For many "high" slip-rate (>5–10 mm/yr) strike-slip faults around the world, geologic slip-rate measurements and strain accumulation rates across faults inferred from geodesy, commonly called "geodetic slip rates," generally agree. For example, the geologic and geodetic rates are generally consistent along the central Altyn Tagh [Cowgill *et al.*, 2009; Elliott *et al.*, 2008; Gold *et al.*, 2009; Gold *et al.*, 2011; Wallace *et al.*, 2004], central and eastern Kunlun [e.g., Gold and Cowgill, 2011; Harkins and Kirby, 2008; Kirby *et al.*, 2007; Van der Woerd *et al.*,

2002; Zhang *et al.*, 2004], and North Anatolian [e.g., Hubert-Ferrari *et al.*, 2002; McClusky *et al.*, 2000] faults, as well as along many of the straight, single-strand sections of the San Andreas fault, such as the Carrizo segment [e.g., Schmalzle *et al.*, 2006; Sieh and Jahns, 1984].

In contrast, there are numerous examples where slip-rate estimates derived from geology and geodesy disagree, especially across shear zones that contain numerous, discontinuous faults. For example, across the Marlborough fault system on the South Island of New Zealand, geodetic strain accumulation rates for the Wairau and Hope faults are 9 mm/yr and 19 mm/yr [Bourne *et al.*, 1998], respectively, whereas the geologic slip rates are 3–5 mm/yr [Knuepfer, 1992] and 10–14 mm/yr [Cowan, 1990; Cowan and McGlone, 1991], respectively. The Eastern California Shear Zone and Walker Lane, a zone of dextral shear along the eastern side of the Sierra Nevada, are also noted for such apparent discrepancies. This region accommodates 15–25% of the modern strain associated with the ~50 mm/yr of dextral motion between the Pacific-North American plate relative motion [Dixon *et al.*, 2000; Hammond and Thatcher, 2007; Hammond *et al.*, 2011; Lifton *et al.*, 2013; Thatcher, 2003]. Geodetic measurements record substantially more right-lateral shear than counterpart geologic studies have documented. For example, in the Eastern California Shear Zone south of the Garlock fault, geologic slip rates account for only one half of the geodetic strain accumulation rate [e.g., Herbert *et al.*, 2013; Oskin *et al.*, 2008; Shelef and Oskin, 2010]. Across the left-lateral Garlock fault, geodetic surveys identify little-to-no sinistral strain accumulation [Meade and Hager, 2005; Peltzer *et al.*, 2001], whereas late Quaternary geologic studies indicate a slip rate of 5–7 mm/yr [e.g., Ganey *et al.*, 2012; McGill and Sieh, 1993]. Explanations for these types of discrepancies include off-fault deformation [e.g., Dolan and Haravitch, 2014; Herbert *et al.*, 2013], transients related to the seismic cycle or ductile fault structure at depth [e.g., Kenner and Simons, 2005; Oskin *et al.*, 2008], earthquake clustering [e.g., Marco *et al.*, 1996], and intrafault communication [e.g., Ambraseys, 1971; Dolan *et al.*, 2007; Gold *et al.*, 2013a].

In this investigation, we focus on the northern Walker Lane (NWL) (Figure 1), a region of distributed dextral deformation north of Reno, NV, and Truckee, CA, where the total contemporary dextral strain accumulation rate is constrained by geodetic surveys at ~7 mm/yr [Hammond *et al.*, 2011]; this value is at least twice as much as the total budget of 1.4–3.3 mm/yr of dextral-slip rate documented by geologic studies along the Mohawk Valley [Sawyer *et al.*, 2013], Grizzly Valley [Gold *et al.*, 2013b], Honey Lake [Turner *et al.*, 2008; Wills and Borchardt, 1993], and Warm Springs faults [Gold *et al.*, 2013a]. The Mohawk Valley fault zone (MVFZ), the westernmost Quaternary fault in the NWL, has limited published data on its record of Quaternary slip. The lack of information on MVFZ is particularly significant, given recent block models based on geodetic data that indicate this system may accumulate as much as 2.9 ± 0.2 mm/yr [Hammond *et al.*, 2011] or 5 mm/yr [Dixon *et al.*, 2000] of region dextral strain, substantially more than a minimum Holocene slip rate of 0.4 ± 0.1 mm/yr, reported by Sawyer *et al.* [2013].

We conducted a detailed investigation of the Quaternary faulting on the MVFZ to document the Holocene record of earthquakes. We used high-resolution airborne light distance and ranging (lidar) data and field observations to map this fault system in greater detail than previously documented. Based on this mapping, we selected a site near Sulphur Creek for paleoseismic investigation. From this study, we present evidence for four latest Quaternary surface-rupturing earthquakes, indicating that the MVFZ plays a significant role in accommodating dextral shear in the NWL. However, our results suggest a geologic deformation rate that is inconsistent with the strain accumulation rate (2.9 ± 0.2 mm/yr) inferred from regional geodetic modeling. We hypothesize that the discrepancy may indicate that unidentified faults are accommodating some of the regional shear.

2. Geologic Framework

The 60 km long, north-northwest trending Mohawk Valley fault zone extends from Sierraville, CA, in southwestern Sierra Valley along the Middle Fork of the Feather River to the American Valley near Quincy, CA [Sawyer *et al.*, 2013; Turner, 1897]. The MVFZ defines the eastern margin of the Sierra Nevada and is the westernmost of a series of active structures that form the NWL [Henry *et al.*, 2007] (Figure 1). To the south, the MVFZ is kinematically linked to the Truckee and Polaris faults [Hunter *et al.*, 2011; Melody *et al.*, 2012; Olig *et al.*, 2005; Slack *et al.*, 2011]. To the north, the MVFZ may be kinematically linked with the Indian Valley and Butt Valley faults [Page *et al.*, 1997].

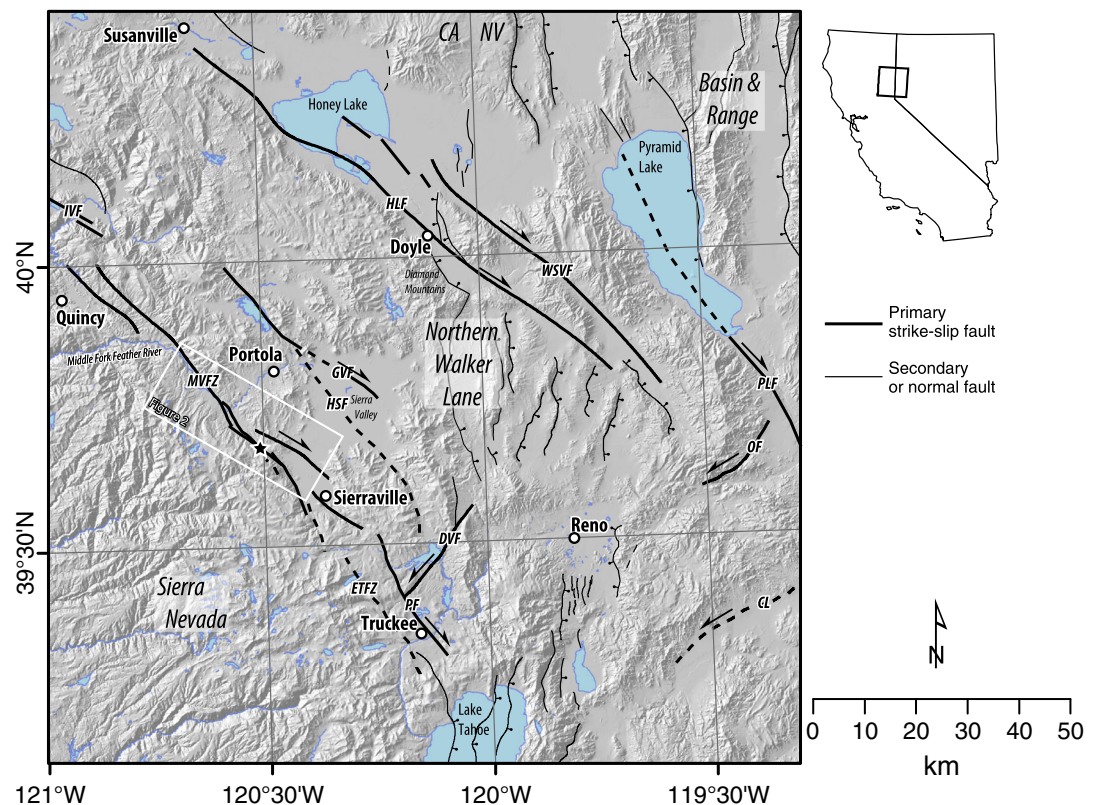


Figure 1. Map of the northern Walker Lane study area and regional strike-slip and normal faults, simplified from the U.S. Geological Survey, Nevada Bureau of Mines and Geology, and California Geological Survey [2006], *Faulds and Henry* [2008], the California Department of Water Resources [1963], *Saucedo and Wagner* [1992], *Hunter et al.* [2011], *Gold et al.* [2013a, 2013b], *Olig et al.* [2005], and our mapping using lidar data and field observations. Abbreviations: CL, Carson Lineament; DVF, Dog Valley fault; ETFZ, East Truckee fault zone; GVF, Grizzly Valley fault; HLF, Honey Lake fault; HSF, Hot Springs fault; IVF, Indian Valley fault; MVFZ, Mohawk Valley fault zone; OF, Olinghouse fault; PF, Polaris fault; PLF, Pyramid Lake fault; and WSVF, Warm Springs Valley fault. Arrows indicate relative direction of strike-slip fault movement. Bar and ball indicates down-thrown block of normal faults. Star depicts location of Sulphur Creek site.

The MVFZ was first mapped by *Turner* [1897]. Subsequent mapping by *Saucedo and Wagner* [1992], *Grose* [2000], and *Redwine* [2013] defines four principal rock types cut by the MVFZ: Paleozoic metamorphic rocks, Jurassic-Cretaceous Sierran granodiorite, Miocene-Pliocene volcanic rocks, and Quaternary glacial, fluvial, and lacustrine deposits. The MVFZ is interpreted as a high angle, dextral to normal slip fault zone [*Sawyer et al.*, 2013]. The MVFZ vertically offsets the 16 Ma Lovejoy basalt and 5 to 3 Ma Mehrten Formation by 500–1180 m down-to-the-northeast [*Sawyer*, 1995, and references therein]. The MVFZ has a net dextral offset of <1 km constrained by a contact between Cretaceous granite and Paleozoic metamorphic rock [*Faulds et al.*, 2005]. The magnitude of this displacement is significantly smaller than offsets documented along nearby strike-slip faults in the region such as the Honey Lake, Warm Springs, and Pyramid Lake faults, which dextrally offset west-trending paleovalleys ~5 km, 8–10 km, and 8–10 km, respectively [*Faulds et al.*, 2005].

The first detailed evaluation of Quaternary faulting along MVFZ was undertaken by *Sawyer et al.* [1993, 1995, 2005, 2013]. Mapped fault traces from their air photo analysis and field-mapping effort are presented in *Olig et al.* [2005]. Those studies interpret the oblique dextral-normal motion on the MVFZ to be partitioned onto separate dextral- and normal-slip faults. South of the town of Clio (Figure 2), there are two primary zones of faulting, a western normal fault zone and an eastern dextral fault zone. North of Clio, the distinction between normal and dextral fault traces is less clear.

Paleoseismic studies have been undertaken along the southern MVFZ, where faulting is distributed across two distinct and subparallel faults separated by 4–4.5 km, including the Calpine site on the western strand

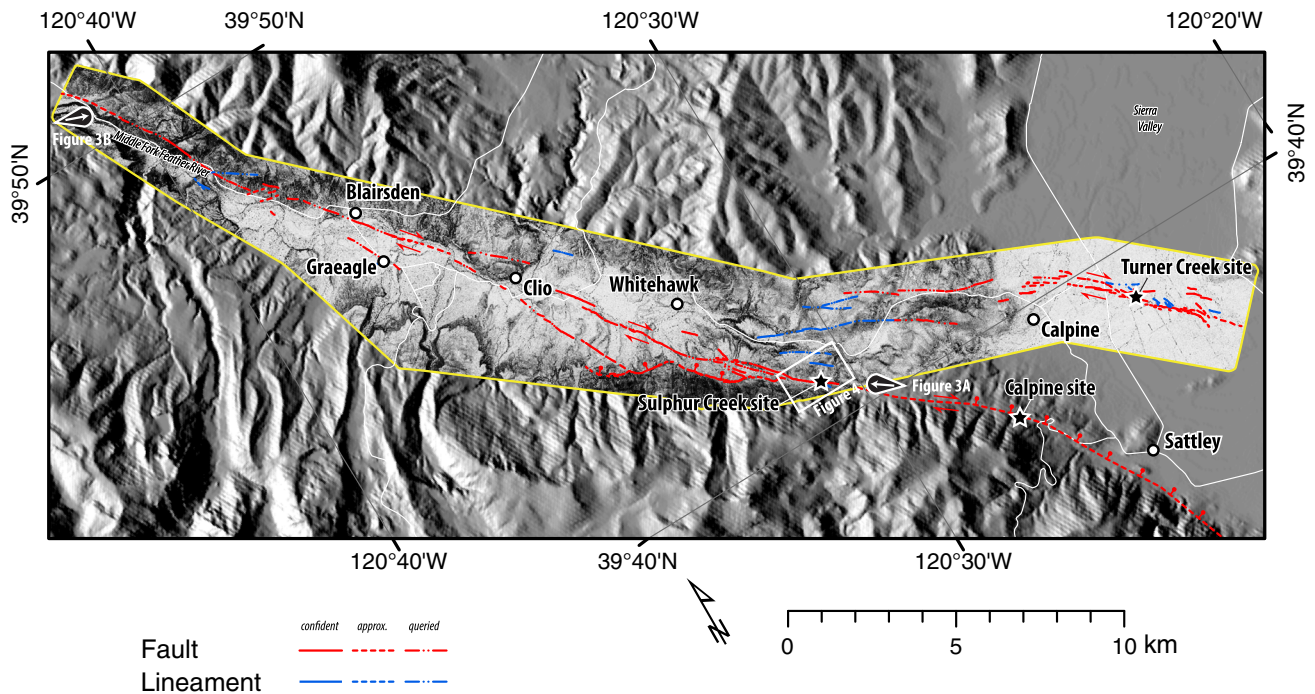


Figure 2. Overview of the Mohawk Valley fault zone with our mapping of faults and lineaments from lidar data and field observations. Base map includes hill shade image derived from 10 m National Elevation Data Set (NED) and slope shade image derived from 0.25 m lidar data set along the MVFZ (yellow outline). Regional road network indicated with white lines. Trace of MVFZ in southwest portion of map, with NED coverage, simplified from *Olig et al.* [2005].

[Sawyer et al., 1993] and the Turner Creek site on the eastern strand [Sawyer et al., 2013]. The western strand is interpreted to be a dominantly normal fault that has experienced four mid-to-late Pleistocene surface-faulting earthquakes prior to 12 ka. Sawyer et al. [2013] interpret the eastern strand to be dominated by dextral faulting, and their preliminary results indicate that the fault has had three latest Quaternary surface-rupturing earthquakes. Furthermore, the Turner Creek study places a minimum bound on the dextral-slip rate of 0.4 ± 0.1 mm/yr based on a right-lateral offset of a buried channel. The rate is likely a minimum because the fault is composed of multiple strands at the trench location and because the site is near the southern terminus of the fault.

3. Fault Trace

3.1. Methods

We mapped the central and southern portions of the MVFZ using field-based observations and analysis of a 131 km² swath of high-resolution (15–17 pulses/m²) airborne lidar data (Figure 2). We focused our analysis on a 0.25 m resolution bare-Earth digital elevation model (DEM) derived from those data. The lidar data are publicly available from OpenTopography (www.opentopography.org), where additional details on acquisition, processing, and accuracy can also be found. The lidar data enhanced our ability to identify subtle topographic evidence of faulting, which is commonly obscured by the dense tree canopy in the region.

3.2. Mapping Results

In general, our mapping (Figures 2–4) is similar to that presented in *Olig et al.* [2005] but we propose a simpler array of active fault strands. We restrict our mapping to the extent of lidar coverage. We identified numerous lineaments, scarps, and other potential tectonic features in the Mohawk Valley region, and we discuss those results from south to north.

In Sierra Valley, the lidar coverage was restricted to the eastern trace of the MVFZ that was previously trenched by Sawyer et al. [2013], and here the fault is expressed as a southwest facing, 0.8 m high escarpment. In Sierra Valley, a fluvial system drains toward the northeast and is impounded against the escarpment. This

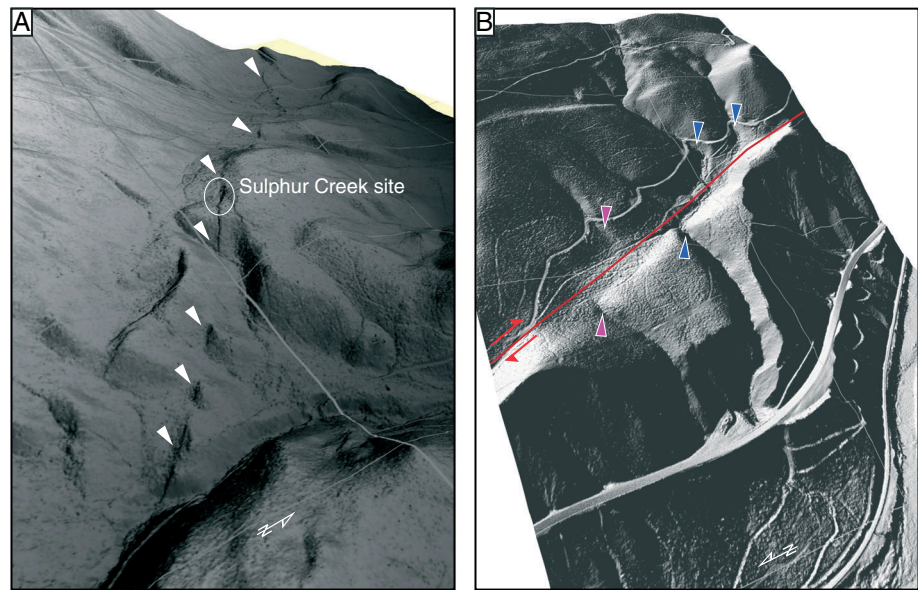


Figure 3. (a) Perspective view of western strand of the Mohawk Valley fault zone and the Sulphur Creek site. Upslope and west facing escarpments define the fault trace, which are indicated by gray triangles. (b) Perspective view of laterally offset (pink arrows) and deflected (blue arrows) drainages along trace of the MVFZ near northern extent of lidar. Arrows indicate possible drainage correlations across the fault. Image is derived from 0.25 m lidar data. Location and look direction of images are indicated in Figure 2. Gridline spacing in images is 500 m.

fault trace is interpreted as a dextral-slip fault system [Sawyer *et al.*, 2013], but due to the uphill-facing nature of the scarp, no consistent series of lateral offsets are observed on the valley floor.

North of Sierra Valley ~2 km northwest of Calpine (Figure 2), the expression of the eastern fault strand becomes increasingly subdued near the drainage divide between Sierra Valley and the Sulphur Creek drainage. Probable surface faulting is weakly expressed as tonal lineaments in aerial photographs, and small discontinuous escarpments may be of tectonic origin. In contrast, the western fault trace at this latitude is well expressed as an alternating uphill- or downhill-facing, continuous linear escarpment. We note numerous locations where the fault right-laterally offsets landforms (Figures 3–5). Based on these observations, we interpret the western fault strand to be dominantly right lateral. Well-preserved scarp morphology suggests that this section of fault records the most recent surface rupture associated with the MVFZ.

At approximately 4 km southeast of Whitehawk, the western fault strand branches. The strike-slip fault strand continues along the same 325° trend, while an arcuate splay with a 2–7 m high, northeast facing escarpment trends to the west before again curving north. We interpret this westernmost, arcuate fault trace to be a predominantly normal-slip fault on the basis of the apparent lack of lateral offsets along this reach, its range front position, and its scalloped map pattern.

Between Whitehawk and Clio, the normal fault trace becomes increasingly subdued, and it appears to transfer slip to a prominent linear strand that cuts northward across the floodplain of the Feather River to near Clio. At Clio this strand continues to Blairsden, with a short subparallel (2 km) strand near Graeagle. North of Blairsden, the surface trace of the MVFZ evident in the lidar data is discontinuous and subdued; this may be caused by erosion of the main fault trace in the active channel and floodplain of the Feather River or by active slope processes that have obscured the evidence of young faulting. One exception is near the northwestern extent of our map area, where a strand of the MVFZ has created a side-hill bench on the hillslope east of the Feather River and right-laterally deflected and/or offsets two or more channels (Figure 3b).

4. Trench Setting, Structure, and Stratigraphy

We selected the Sulphur Creek site for paleoseismic investigation. The site is located on the western strand of the MVFZ, where there is a well-preserved fault scarp. Although we note numerous lineaments (blue lines,

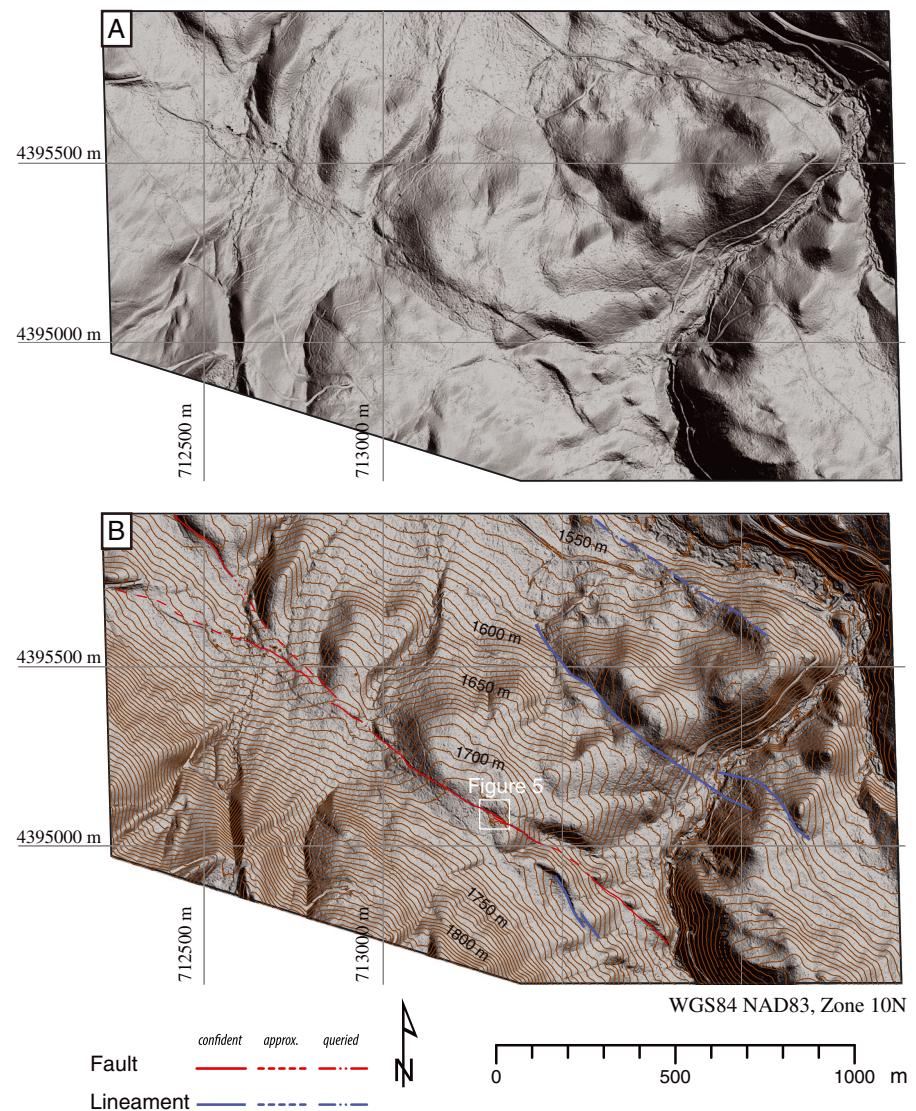


Figure 4. Detailed (a) lidar topographic map and (b) fault (red) and lineament (blue) map of the western strand of the Mohawk Valley fault zone centered on the Sulphur Creek site. In Figure 4b, contour interval is 5 m. Many of the north-west-oriented lineaments apparent in Figure 4a are surface disturbances from regional logging.

Figure 2) that overlap with this fault trace, we find no evidence for lateral or vertical displacement that would lead us to conclude that they are late Quaternary fault traces. One particularly suspicious feature is a right-curving ridge, of possible glacial origin, located ~200 m southeast of the Sulphur Creek site. This ridge has a steep uphill-facing escarpment; unfortunately, field relationships did not allow us to determine if this is a tectonic or some other erosional/mass-wasting escarpment. Drainages do not appear to be deflected across this feature. Furthermore, even if the uphill-facing escarpment (blue, Figure 4) is a fault scarp, it coalesces with the main trace of the MVFZ south of the Sulphur Creek site; so it does not appear that faulting bypasses our study site. In summary, the geomorphic evidence supports our interpretation that, at this latitude, dextral motion along the MVFZ is concentrated on this strand of the fault.

The Sulphur Creek site is a closed depression along a well-preserved, continuous and nondistributed trace of the MVFZ. The depression at the site captures fine-grained pond sediment that interfingers with coarser clastic debris shed from a bedrock-colluvium fault scarp along the northeast margin of the closed depression (Figures 4 and 5). The closed depression floods annually during spring snow melt (Figure 6a) but dries later in the summer (Figure 6a). This northwest oriented, oblong, closed basin is located on the western slope of

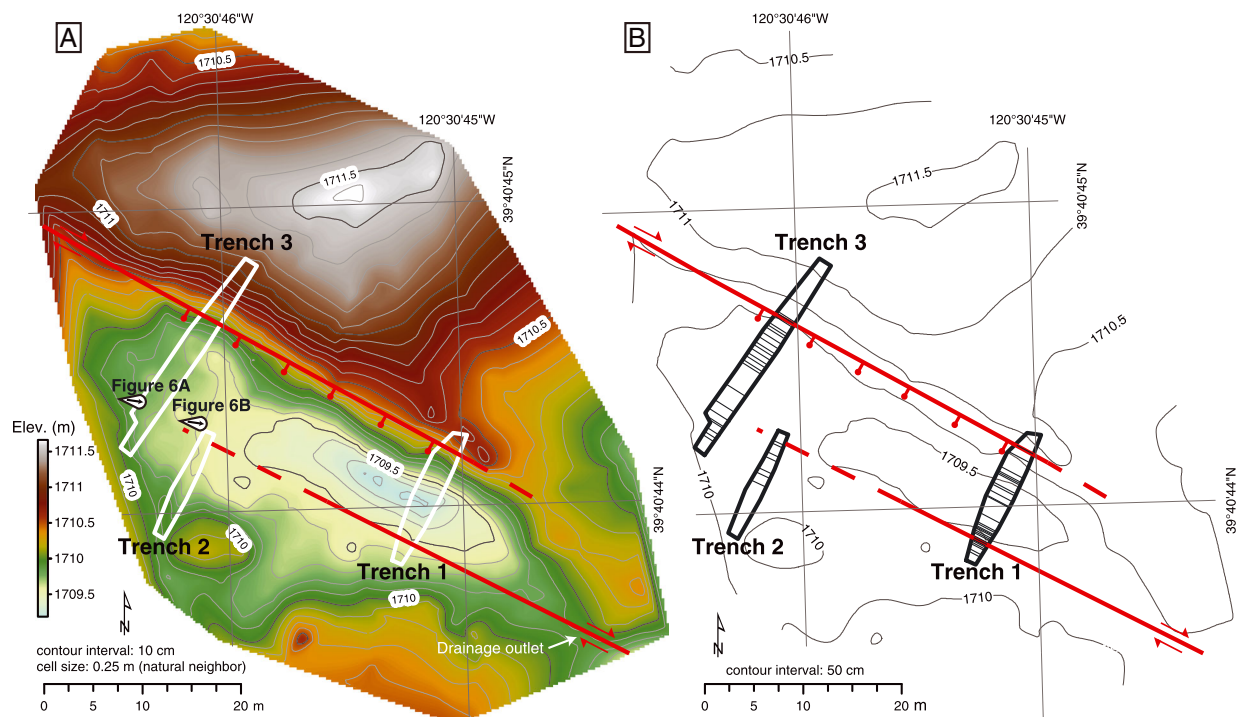


Figure 5. (a) Topographic map of the Sulphur Creek site along the western trace of the Mohawk Valley fault zone. Map derived from integrated total station and Real-Time Kinematic GPS survey of the site. At the site, oblique dextral-normal faulting has produced a closed depression that we interpret to be related to an extensional, right stepover between two active strike-slip strands of the MVFZ. White outlines show locations of three fault-perpendicular trenches excavated at the site. (b) Simplified topographic map, depicting fault density (black lines) observed in trench exposures.

Mohawk Valley, about 185 m above the valley floor. The basin is approximately 45 m long, 15 m wide, and at its deepest point is 0.7 m below the local stream outlet at the southeastern margin of the depression. A 1.0 to 1.5 m high uphill-facing escarpment defines the basin's northeastern margin. We interpret the basin to result from an extensional, right stepover between two active strike-slip strands of the MVFZ, as depicted in Figure 5. We excavated three fault-perpendicular trenches across the basin and exposed fine-grained pond sediment that interfingers with multiple wedges of colluvium derived from the bedrock-colluvium scarp, which bounds the northeastern side of the pond. We interpret the stratigraphy of the exposed sediments to reflect a history of basin closure and breaching, which has largely been controlled by faulting. Below, we summarize the structures and stratigraphy in the trenches; see Figure 7 for maps of trenches 1 and 3. Large-format versions of all three trench logs and trench photo mosaics are in the supporting information.

4.1. Structure

We observed faults in all three trenches. Fault strands that have significant vertical displacement and/or significant unit thickness changes (which indicate normal and dextral faulting, respectively) were present only in trenches 1 and 3 (Figure 7), and we concentrate our discussion on these trenches. Along the normal fault strands that define the northeastern basin margin, we measured vertical displacements of greater than 50 cm, and these vertical displacements are commonly associated with scarp-derived colluvial deposits on the downthrown side of the fault. Along the basin axis and parallel to the strike of the MVFZ, subvertical fault density steps to the right from the south to north across the basin (Figure 5b).

In trench 1, we exposed a 40° southwest dipping, normal fault, fault zone 1 (FZ1) and three zones (FZ2–FZ4) of penetrative, vertical faults that we interpret to be strike-slip fault strands on the basis of measurable changes in the thickness of stratigraphic units across these sets of structures (Figure 7). In trench 2, we observed only minor faults that have minimal vertical offsets or unit thickness changes, which we interpret as evidence for minimal normal and lateral faulting, respectively (supporting information). In trench 3, the boundary (FZ1) between the bedrock (unit 8) and basin fill (units 1–7) was marked by several subvertical fault strands, in



Figure 6. Photographs of the Sulphur Creek site showing conditions in the (a) spring during snowmelt when the pond floods and (b) fall when the site is dry. During our work in September 2012, the trenches remained dry to the maximum trench depth about 3 m below the surface.

contrast to the bedrock-basin fill boundary in trench 1, in which this boundary was marked by a gently dipping normal fault. The subvertical fault strands that separate the bedrock from basin fill in trench 3 have a substantial down-to-the-southwest motion, indicating a significant component of normal slip. We interpret the bedrock-basin fill contact (FZ1) in trenches 1 and 3 to correlate (Figure 5). To the southwest in trench 3, within the basin axis, sets of subvertical faults (FZ2–FZ4) juxtapose units of variable thickness, which we interpret to result from strike-slip motion.

4.2. Stratigraphy

The trenches expose three general categories of deposits: weathered and deformed bedrock; interbedded gravel, sand, and silt we interpret as pond sediment with intermittent fluvial reworking; and poorly sorted, weakly stratified packages of diamict that we interpret as fault scarp-derived colluvial deposits. The deposits can be subdivided into distinct units, and these units are readily correlated between all three trenches on the basis of color, texture, sedimentary structure, thickness, and stratigraphic position. The correlations are corroborated by radiocarbon and luminescence dating described below. Unit 8 is pervasively sheared, weathered, and oxidized, maroon-colored

granodiorite that was exposed at the northeastern ends of trenches 1 and 3 and forms the northeastern margin of the depression. Unit 7 consists of massive, grayish yellow-brown sand (10YR 6/2, moist Munsell color) with minor silt and is the stratigraphically lowest basin fill unit exposed, observed only in trenches 1 and 3. Unit 6 is massive, yellow-orange silty clay (10YR 6/3) with occasional sand lenses. Unit 5 consists of upward coarsening, massive, clay-rich sand (10YR 6/6) that contains scattered yellow-brown gravel lenses. In trench 3, we subdivided the unit. Unit 5a is characterized by sandy mottled clay with some yellowish brown silt whereas unit 5b is characterized by pebbly mottled clay with dull yellow-orange silt and sand with angular pebbles. We interpret units 5–7 to record low-energy lacustrine deposition with minor pulses of moderate energy fluvial input (e.g., sand in unit 7). We identified unit 4 only in trenches 2 and 3 where it consists of a layer of angular to subangular cobbles in a silty sand matrix (7.5YR 6/6). The cobbles are more abundant in the southwestern end of the trenches, closer to the center of the depression. We interpret unit 4 to be a debris flow derived from the hillslope southwest of the site. Unit 3b is composed of moderately sorted, orange, fine-to-medium grained feldspar sand (2.5YR 6/2) and was exposed only in trenches 2 and 3. Unit 3a consists of moderately sorted, dark gray to brown, medium-grained feldspar sand (10YR 5/4) and was exposed only in trench 1. Units 3a and 3b likely record a through-going fluvial system, perhaps at a time when the basin was not internally drained. Unit 2b consists of massive silt with minor fine sand (10YR 3/4) and was exposed only in trenches 2 and 3. Unit 2a is composed of massive to weakly bedded silt and coarse sand (10YR 5/8) and was present only in trench 1. Unit 1 consists of bright, yellowish brown, weakly laminated silt (10YR 3/3) with

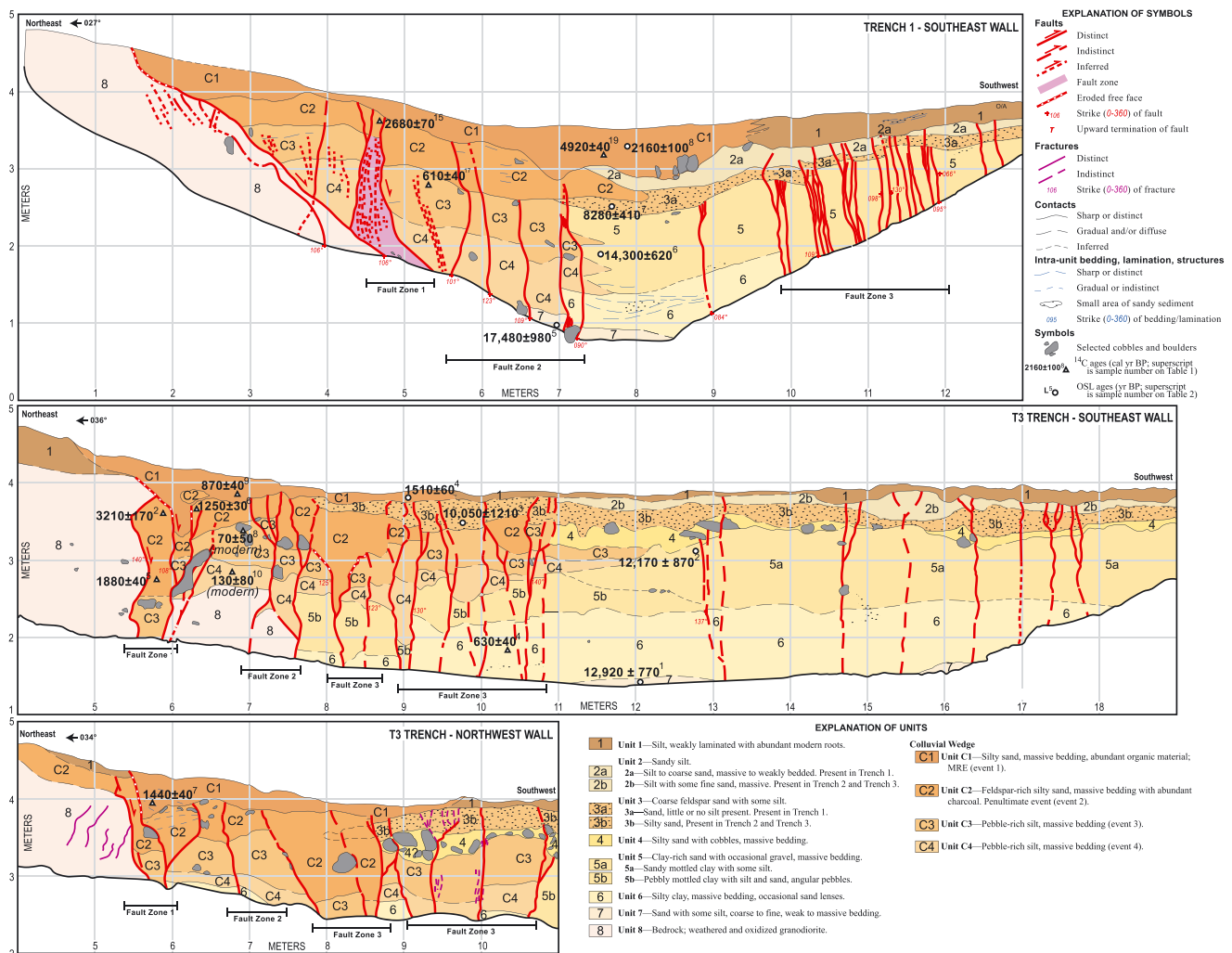


Figure 7. Simplified trench logs from the Sulphur Creek site along the Mohawk Valley fault zone. Detailed, large-format versions of the logs and companion photo mosaics are in the supporting information.

abundant roots and corresponds to the modern, organic-rich, A-horizon that is forming at the ground surface. We interpret units 1, 2a, and 2b to record low-energy lacustrine deposition, associated with a closed basin.

Along the southwest facing escarpment at the pond's northeastern edge, we exposed four poorly sorted and weakly stratified diamicts (C1–C4) in trenches 1 and 3. We interpret these units as scarp-derived colluvium because they are adjacent to, or cut by, fault strands and they interfinger with pond sediment and pinch out toward the center of the basin. Units C4 and C3 consist of massive, yellow-orange, pebble-rich silt (C4, 10YR 5/6; C3, 10YR 6/4). We mapped the boundary between the colluvial packages on the basis of a series of aligned, small clasts, which we interpret to be a stone line marking a period of temporary surface stability (see note 3 on southeast trench wall in Figure S2 in the supporting information). Unit C2 consists of massive, charcoal-rich, yellow-orange, feldspar-rich, silty sand (10YR 6/3) and was distinctive and thus easily correlated between trenches 1 and 3. Unit C1 consists of poorly indurated, massive, silty brown sand (10YR 3/4). Similar to unit C2, unit C1 was easily correlated between trenches 1 and 3. Unit C1 interfingers and merges with unit 1 in both the upslope (trench 3) and downslope directions.

5. Samples and Dating

We used radiocarbon and optically stimulated luminescence (OSL) dating to estimate the depositional ages of colluvial (units C1–C4), lacustrine (units 1, 2, 5, 6, and 7), and fluvial (units 3 and 4) deposits in the trenches.

Table 1. Radiocarbon Data From the Sulphur Creek Site, Mohawk Valley Fault Zone

Sample ID	Lab No. ^a	Fraction Modern	Error	$\Delta 13C$	Reported Age ^b (¹⁴ C year B.P.)	Calibrated Age ^c (cal year B.P.)	Mean	1 σ	Sample Type ^d
MSCB-R2	OS-102392	0.68460	0.01160	−25.06	3040 ± 140	3560–2860	3210	170	Conifer, charcoal, 2–3 fragments
MSCB-R4	OS-101968	0.91950	0.00220	−23.02	675 ± 20	680–560	630	40	<i>Pinus</i> , friable charcoal, 1 fragment
MSCB-R5	OS-101969	0.78590	0.00290	−26.07	1930 ± 30	1950–1810	1880	40	<i>Pinus</i> , charcoal, 2 fragments
MSCB-R6	OS-101970	0.84980	0.00210	−23.87	1310 ± 20	1300–1180	1250	30	<i>Abies</i> , charcoal, 1 fragment
MSCB-R7	OS-101971	0.82520	0.00200	−24.22	1540 ± 20	1520–1370	1440	40	Conifer, Incompletely charred, 1 fragment
MSCB-R8	OS-101972	0.99610	0.00240	−26.51	30 ± 20	250–30	70	50	Microcharcoal
MSCB-R9	OS-101974	0.88660	0.00220	−23.03	965 ± 20	930–790	870	40	Conifer cone fragment, charred, 1 fragment
MSCB-R10	OS-101973	0.98590	0.00310	−26.96	115 ± 25	270–10	130	80	Microcharcoal
MSCB-R13	OS-101975	0.23010	0.00160	−25.17	11800 ± 55	13800–13450	13640	90	<i>Pinus</i> , charcoal, 2 fragments
MSCB-R15	OS-101976	0.72770	0.00180	−24.08	2550 ± 20	2750–2510	2680	70	<i>Pinus</i> , vitrified charcoal, 1 fragment
MSCB-R17	OS-101977	0.92150	0.00220	−27.69	655 ± 20	670–560	610	40	Microcharcoal
MSCB-R19	OS-101978	0.58080	0.00180	−23.51	4360 ± 25	5030–4850	4920	40	Conifer, charcoal, 1 fragment

^aNational Ocean Sciences Accelerator Mass Spectrometry Facility, Woods Hole Oceanographic Institution.^bAnalytical uncertainties (1 σ) reported by accelerator mass spectrometry laboratory.^cCalibrated age range (95.4%); calibration from computer program OxCal (version 4.2.) [Bronk Ramsey, 2008, 2009] and the IntCal 2009 atmospheric data set [Reimer et al., 2009].^dSample identification performed by PaleoResearch Institute.

Ages from the two methods generally agree. The radiocarbon ages provide constraints on the timing of the most recent earthquakes, whereas the luminescence ages place constraints on the time interval for the late Quaternary faulting record. In the text, we present radiocarbon and luminescence age uncertainties at the 1 σ level.

5.1. Radiocarbon

We processed 12 samples of organic material for accelerator mass spectrometry radiocarbon (¹⁴C) dating. The samples were preprocessed by PaleoResearch Institute (PRI) to mechanically separate the target organic material from inorganic sediment and to identify the plant material to the genus or species level, when possible. For three samples, PRI concentrated microcharcoal from bulk sample aliquots; however, all of these microcharcoal samples yielded modern or near-modern ages, discussed below. Following preprocessing, we submitted the samples to Woods Hole Oceanographic Institute for final processing and dating. The results are shown in Table 1.

Our radiocarbon analyses yielded mixed results. Seven of our 12 analyses yielded ages that are apparently either too young (samples Mohawk Sulphur Creek Bench (MSCB)-R4, MSCB-R6, MSCB-R8, MSCB-R10, and MSCB-R17) or too old (MSCB-R13 and MSCB-R19) for their stratigraphic position when compared to the luminescence ages discussed below. We attribute the apparently young ages to unrecognized burrowing and root penetration (MSCB-R4 and MSCB-R6), and in the case of our three microcharcoal samples (MSCB-R8, MSCB-R10, and MSCB-R17) to burrowing and infiltration of microcharcoal from the modern surface down through the local soil column. We attribute apparently anomalously old ages to recycling of detrital charcoal from deposits on the steep forested slopes surrounding the closed depression. These problematic samples are identified as outliers in the age-event/stratigraphy plot presented in the supporting information (Figure S1); so we excluded all of these samples from further analysis.

5.2. Luminescence

For our eight luminescence samples, we measured OSL on fine sand-size quartz grains to constrain the depositional age of sediments exposed in the trenches [e.g., Duller, 2008; Personius et al., 2009]. To process the samples, we used the single aliquot regeneration protocol to measure equivalent dose. The OSL technique estimates the time when sediments were last exposed to sunlight, which presumably occurred when the eroded sediment was being transported to its present depositional site [Duller, 2008]. We provide the luminescence parameters in the supporting information. We calculated the dose rate for each sample by using a high-resolution gamma ray spectrometer to measure the radiation emitted from the bulk sediment we collected around each luminescence sample [Snyder and Duval, 2003]. We present the luminescence results in Table 2.

Table 2. Quartz OSL Data and Ages From the Sulphur Creek Site, Mohawk Valley Fault Zone

Sample Information	Percent Water Content ^a	K (%) ^b	U (ppm) ^b	Th (ppm) ^b	Cosmic Dose ^c Additions (Gy/ka)	Total Dose Rate (Gy/ka)	Equivalent Dose (Gy)	<i>n</i> ^d	Age (years) ^e
<i>Trench 3</i>									
MSCB-L1	15 (32)	2.70 ± 0.04	2.02 ± 0.29	5.84 ± 0.39	0.21 ± 0.02	3.02 ± 0.10	39.0 ± 1.95	25 (30)	12,920 ± 770
MSCB-L2	10 (55)	2.73 ± 0.03	1.44 ± 0.09	5.28 ± 0.22	0.26 ± 0.02	2.63 ± 0.07	32.1 ± 2.15	20 (30)	12,170 ± 870
MSCB-L3	5 (48)	4.16 ± 0.06	3.89 ± 0.35	13.7 ± 0.59	0.29 ± 0.02	5.32 ± 0.13	53.5 ± 6.31	4 (20)	10,050 ± 1,210
MSCB-L4	2 (44)	2.66 ± 0.03	2.47 ± 0.11	6.17 ± 0.22	0.37 ± 0.03	3.45 ± 0.08	5.23 ± 0.16	25 (30)	1,510 ± 60
<i>Trench 1</i>									
MSCB-L5	21 (46)	2.76 ± 0.04	3.33 ± 0.12	10.9 ± 0.30	0.21 ± 0.02	3.33 ± 0.11	58.2 ± 2.58	24 (25)	17,480 ± 980
MSCB-L6	5 (56)	2.50 ± 0.04	1.90 ± 0.17	6.63 ± 0.32	0.24 ± 0.002	2.55 ± 0.07	36.5 ± 1.17	21 (30)	14,300 ± 620
MSCB-L7	5 (38)	4.06 ± 0.05	2.77 ± 0.23	10.8 ± 0.56	0.26 ± 0.02	4.97 ± 0.14	41.2 ± 1.73	15 (30)	8,280 ± 410
MSCB-L8	9 (51)	2.17 ± 0.04	2.11 ± 0.18	6.73 ± 0.46	0.33 ± 0.03	2.92 ± 0.11	6.30 ± 0.16	20 (24)	2,160 ± 100

^aField moisture with figures in parentheses indicating the complete sample saturation %. Ages calculated using approximately 75% of total saturation values.

^bAnalyses obtained using high-resolution lab gamma spectrometry (Ge detector).

^cCosmic doses and attenuation with depth were calculated using the methods of Prescott and Hutton [1994]. See text for details.

^dNumber of replicated equivalent dose (De) estimates used to calculate the equivalent dose. Figures in parentheses indicate total number of measurements included in calculating the represented equivalent dose and age using radial plots (weighed mean). Dispersion was generally moderate (30%).

^eDose rate and age for fine-grained 250–180 μm sized quartz. Exponential + linear fit used on equivalent dose, errors to 1 σ.

Most of our luminescence samples yielded ages that are in the correct stratigraphic order. The oldest and stratigraphically lowest luminescence samples from trenches 1 and 3 yielded ages of 17.5–12.9 ka (unit 7). The youngest luminescence ages range between 2.1 and 1.5 ka from samples collected at the shallowest stratigraphic position in the trench exposure (unit C1). The luminescence ages are mostly in agreement between trenches 1 and 3. Furthermore, the shallowest (youngest) luminescence ages are generally consistent with the radiocarbon ages from similar stratigraphic positions. Luminescence sample MSCB-L3 (unit 3b) is problematic because it has a dim equivalent dose signal, and thus, only 4 aliquots of 20 provided meaningful results. Because the precision or confidence level in the resulting age of sample MSCB-L3 is poor, we disregard it in our subsequent analysis.

6. Paleoseismology

6.1. OxCal Method

We used Bayesian analysis of the stratigraphic, structural, and geochronologic data in the modeling tool OxCal v4.2.2 [Bronk Ramsey, 2008, 2009; Reimer et al., 2009] to place constraints on the timing of surface ruptures at the Sulphur Creek site. This approach takes into account the relative stratigraphic position of age control and the associated uncertainties in the age information. OxCal applies a Monte Carlo approach to develop a distribution of possible solutions that are quantified via probability distribution functions (pdfs). After removing outliers (Figure S1), we modeled the deposition of sedimentary units as a series of “phase” commands and the intervening surface ruptures, which we interpret as paleoearthquakes, as “date” commands. We provide the code used to make the computations and a complete model with all age data, including outliers, in the supporting information. Our OxCal model provides 95% confidence interval bounds (2 σ) on the timing of four surface ruptures postdating the deposition of unit 7, the oldest surficial deposit exposed in the trenches (Figure 8, Table 3).

6.2. Sequence of Events

Surface faulting recorded in the trench exposures postdates a period of low-energy fluvial and lacustrine deposition, during which time the well-sorted sand (unit 7) and massive silt (unit 6) were deposited (Figure 7). Luminescence samples MSCB-L1 and MSCB-L5 constrain the depositional age of unit 7 to be 17.5–12.9 ka, and our mapping indicates that the observed surface ruptures occurred after this time. The first surface rupture (E4) recorded in the trenches resulted in (or enhanced a preexisting) a southwest facing escarpment, which was the source of scarp-derived colluvium (unit C4). Unit C4 is thicker in trench 1 than in trench 3, which may indicate more normal displacement in trench 1. A combination of normal and right-lateral faulting associated with E4 may have enhanced pond sediment deposition recorded by unit 5. Unit C4 interfingers with unit 5 (undifferentiated) in trench 1 and overlies unit 5b in trench 3. Luminescence

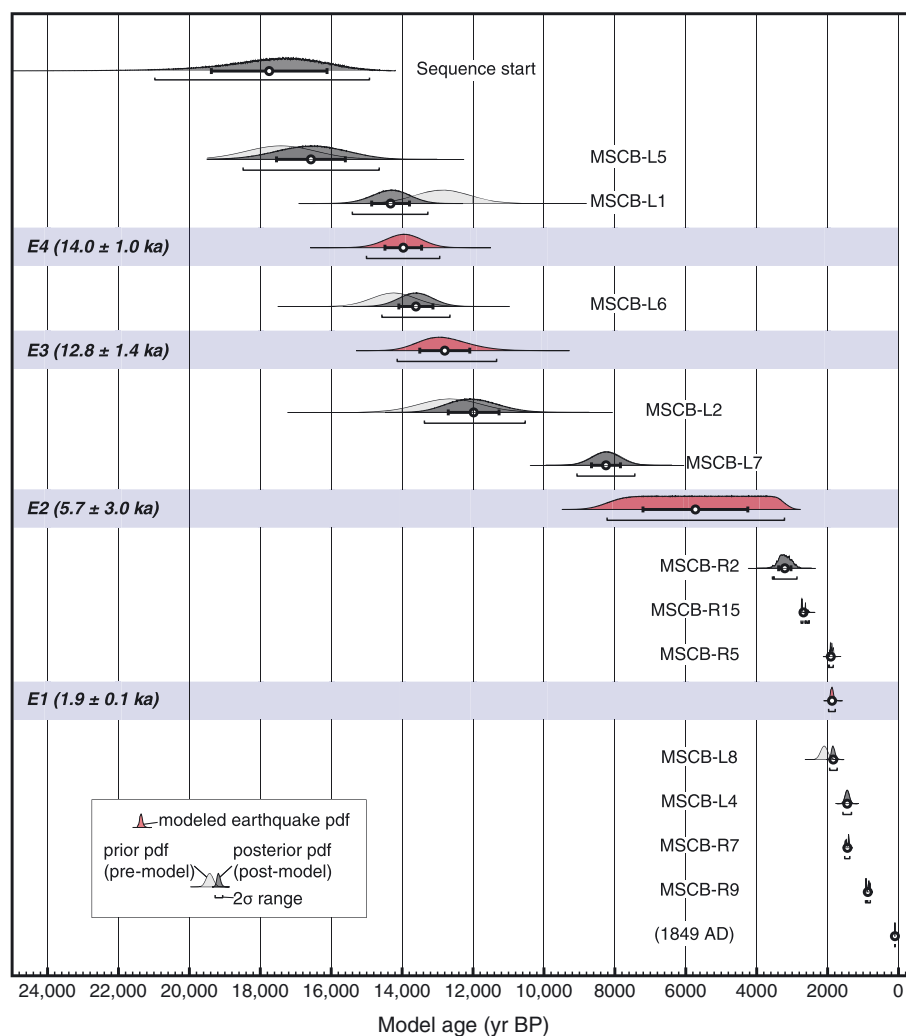


Figure 8. Preferred model from OxCal v4.2.2 [Bronk Ramsey, 2008, 2009; Reimer *et al.*, 2009] of timing constraints on pre-historic surface-rupturing earthquakes (E1–E4) at the Sulphur Creek site on the Mohawk Valley fault zone. Ages listed in sequence are in stratigraphic order, without depth constraints. Prior probability distribution function (pdf) ages are defined by the calibrated radiocarbon and OSL ages. Posterior pdf ages are calculated from the Bayesian OxCal analysis. Historic constraint is from lack of surface-rupturing earthquake since settlement of the region during the California Gold Rush of 1849 A.D. Model with all age constraints and outliers identified is provided in the supporting information.

sample MSCB-L6 places a minimum bound on the time of E4 at 14.3 ka. The OxCal modeling indicates that earthquake E4 occurred 14.0 ± 1.0 ka.

Earthquake E3 occurred near the end of deposition of unit 5. The timing of this earthquake is constrained by luminescence samples MSCB-L6 and MSCB-L2, which are from unit 5 in trenches 1 and 3, respectively. These samples bracket the earthquake to between 14.3 and 12.2 ka. Similar to the previous surface rupture, offset associated with paleoearthquake E3 produced a larger normal displacement in trench 1 than in trench 3, as

Table 3. Earthquake Timing, Sulphur Creek Site, Mohawk Valley Fault Zone

Earthquake	Time Range 95.4% Confidence Level		Mean (year B.P.)	1 σ (year B.P.)	2 σ (year B.P.)	Reported in Text (ka, 2 σ)
	From (year B.P.)	to (year B.P.)				
Earthquake 4	15,010	12,940	13,970	520	1,040	14.0 ± 1.0
Earthquake 3	14,140	11,330	12,800	710	1,420	12.8 ± 1.4
Earthquake 2	8,220	3,210	5,730	1,480	2,960	5.7 ± 3.0
Earthquake 1	1,980	1,780	1,880	50	100	1.9 ± 0.1

evidenced by the thickness of the associated scarp-derived colluvium (C3). Our OxCal modeling yields an earthquake age for E3 of 12.8 ± 1.4 ka.

Surface-rupturing earthquake E2, the penultimate earthquake, occurred following a pulse of high-energy deposition (cobbles, unit 4) and coevally with the deposition of unit 3a, a well-sorted, feldspar-rich sand present in trench 1. In the southeastern part of the basin, E2 produced a surface escarpment and adjacent colluvial package C2 in trench 1. Furthermore, we mapped multiple upward terminations of fault strands in trench 1 near the contact between unit 5 and unit 3a. In trench 3, E2 created a graben, and depocenter at fault zone 3 (horizontal 8 m, vertical 3 m, trench 3 southeast wall) that was filled by scarp-derived colluvium (C2). Constraints on the time of earthquake E2 are broad. A maximum bound of 8.3 ka is from luminescence sample MSCB-L7, which was from the base of unit 3a. A minimum bound of 3.2 ka is from radiocarbon sample MSCB-R2, which was collected in the C2 colluvium. Our OxCal model yields an age of 5.7 ± 3.0 ka for earthquake E2.

The most recent surface-rupturing earthquake (E1) caused about 40 cm of apparent normal displacement on fault zone 1 as well as penetrative vertical faulting and small amounts of down-to-the-northeast displacement on strands in fault zone 3, forming a broad graben near the center of the basin in trench 1 (southeast wall). In trench 3, E1 caused >50 cm of vertical motion along fault zone 1 and penetrative vertical faulting across the basin. We mapped numerous upward shear terminations in trenches 1 and 3 that displace C2 and units 2a and 2b. These upward terminations are strong but not conclusive evidence that helps to define the ground surface at the time of E1. Scarp-derived colluvium (C1) from E1 interfingers with unit 1, which is the modern fill in the pond. The time of earthquake E1 is well constrained by radiocarbon samples from the C2 colluvium (MSCB-R2, MSCB-R5, and MSCB-R15) and radiocarbon and luminescence samples from C1 colluvium (MSCB-L8, MSCB-L4, MSCB-R7, and MSCB-R9). The OxCal model yields an age of 1.9 ± 0.1 ka for earthquake E1.

6.3. Earthquake Recurrence

Paleoearthquake timing derived from our preferred stratigraphic and chronologic model (E4, 14.0 ± 1.0 ka; E3, 12.8 ± 1.4 ka; E2, 5.7 ± 3.0 ka; and E1, 1.9 ± 0.1 ka; Table 3) yields interearthquake recurrence times of 1.2 ± 0.9 kyr between E4 and E3, 7.1 ± 1.6 kyr between E3 and E2, and 3.9 ± 1.5 kyr between E2 and E1. These values yield a closed mean recurrence interval of 4.0 ± 3.0 kyr (1 σ). The open recurrence interval, which includes the open interval from E1 to present day, is 3.5 ± 2.6 kyr (1 σ). The elapsed time since the most recent earthquake, E1, is 1.9 ± 0.1 kyr. We note that the longest interearthquake time (7.1 kyr) is nearly 6 times longer than the shortest time (1.2 kyr). This wide range in interearthquake times could be explained by earthquake clustering, by the possibility that not all large earthquakes on the MVFZ caused surface rupture at the Sulphur Creek site, or because we missed evidence of additional surface ruptures in our trench investigation. However, the consistent presence of four packages of fault scarp colluvium in trenches 1 and 3 supports our interpretation and dating of four surface-rupturing earthquakes at the Sulphur Creek site.

7. Discussion

7.1. Comparison of Results With Turner Creek Site

The chronology of surface-rupturing earthquakes that we determine at the Sulphur Creek site is compatible with results at the Turner Creek site to the southeast (Figure 2), where preliminary results indicate three latest Quaternary earthquakes [Sawyer *et al.*, 2005, 2013]. Earthquake times from the Turner Creek study are as follows: the oldest observed earthquake occurred between 40 ka and 12.7 ka, the penultimate earthquake occurred after 7.8 ka, and the most recent earthquake occurred around or after 2.3 ka. These times at Turner Creek correspond within uncertainty with earthquakes E3 (12.8 ± 1.4 ka), E2 (5.7 ± 3.0 ka), and E1 (1.9 ± 0.1 ka) at the Sulphur Creek site. However, we cannot determine with certainty whether these events were part of the same surface-rupturing earthquakes or are independent.

7.2. Comparison With Geodetic Modeling

There are two primary types of geodetic slip-rate models that have been used to derive slip rates for the MVFZ: elastic block models and faulted continuum models. The elastic block models developed for this region minimize internal block deformation and concentrate slip on block boundaries that coincide with major faults wherever possible. Block models can provide powerful fault slip-rate predictions in situations

where blocks are rigid and fault networks are well characterized [e.g., *McClusky et al.*, 2000; *Meade and Hager*, 2005; *Nyst and Thatcher*, 2004]. For the MVFZ, this approach yields slip rate values that range from 2.6 to 2.9 mm/yr [*Field et al.*, 2013; *Hammond et al.*, 2011]. The faulted continuum models allow for deformation along faults and within the blocks that they bound and yield slip rate values for the MVFZ that range from 0.4 to 0.6 mm/yr (treated as 0.5 ± 0.1 mm/yr, for calculations below) [*Field et al.*, 2013]. However, the continuum models attempt to match geologic slip-rate data, which for the MVFZ includes the minimum 0.4 mm/yr rate reported by *Sawyer et al.* [2013]. This leads a degree of circularity in the continuum models, where input geologic slip rates tend to match output geodetic slip rates; this is by design, but faulty geologic slip rates can skew model results.

To distinguish between the range of predicted slip rates for the MVFZ, we can use results from our paleoseismic investigation at the Sulphur Creek site. The Sulphur Creek site does not preserve stratigraphic or geomorphic features that allow measurement of lateral displacements associated with surface ruptures. However, we can consider the range of slip rates (0.4–2.9 mm/yr) predicted by the GPS models and multiply these values by our average recurrence interval of 4.0 ± 3.0 kyr. If we multiply the slip rate of 2.9 ± 0.1 mm/yr inferred from the GPS block model [*Hammond et al.*, 2011] by our average recurrence interval of 4.0 ± 3.0 kyr, this yields an average slip per event value of 11.6 ± 0.8 m. In contrast, if we multiply the slip rate of 0.5 ± 0.1 mm/yr determined from faulted continuum GPS models by our average recurrence interval of 4.0 ± 3.0 kyr, this yields an average slip per event value of 2.0 ± 0.8 m. A single-event displacement corresponding to the prediction made by the GPS block model (~ 11.6 m) is unlikely. The implied magnitude of an earthquake with a maximum or average displacement value of 11.6 m along a strike-slip fault is M 7.6–8.0 [*Wells and Coppersmith*, 1994], which would be among the largest magnitude strike-slip fault ruptures ever documented. Furthermore, empirical relationships between fault length and maximum slip predict that for a 60 km long, strike-slip fault with a rupture width (depth) of 15 km, typical maximum slip values are 2.4–2.7 m and average slip values are 1.4 ± 0.2 m [*Wells and Coppersmith*, 1994]. These values much more closely match predicted per-event displacements associated with lower slip rates in existing continuum GPS models (2.0 m) and yield more moderate, and reasonable, earthquake magnitudes (M 7.0–7.3). Furthermore, if 11.6 ± 0.8 m of slip per event is accurate, we might predict that the landscape would contain clearly faulted and laterally offset landforms from the most recent surface rupture about 1.9 ka. However, our analysis of the high-resolution lidar data and field observations failed to identify any landforms that record such large single-event displacements.

In comparing our results with the GPS models, we consider the possibility that we may not have captured all of the paleoearthquakes on this section of the MVFZ. Although we cannot rule out this explanation, several lines of reasoning suggest that the paleoearthquake chronology is recorded continuously at the Sulphur Creek site. First, our results are broadly consistent with the faulting history defined by *Sawyer et al.* [2013] at the Turner Creek site, which would make sense if both sites ruptured during the same earthquakes. Second, our mapping suggests that at the latitude of the Sulphur Creek site, all of the deformation appears to be concentrated on a single, western fault strand. Third, the depositional setting of the site is aggradational, without evidence for significant erosion after ~ 14 ka. Finally, the Sulphur Creek site is located along a very well-defined reach of the fault as identified by lidar analysis, at one of the few places where the MVFZ has been active recently along a single strand. These observations favor the interpretation that the record we report is complete. Alternatively, it is useful to consider implications of the geodetically modeled rates at the block boundary corresponding to the MVFZ [*Hammond et al.*, 2011], which predict lateral strain accumulation (2.9 ± 0.1 mm/yr) of approximately 41 m since ~ 14 ka (oldest deposit exposed at Sulphur Creek site). Approximately 16 surface ruptures of ~ 2.55 m, the typical maximum surface rupture associated with a 60 km fault [*Wells and Coppersmith*, 1994], would be required to relieve 41 m of strain accumulation; this decreases to eight events if an outsized surface rupture of 5 m is considered. We consider it unlikely that we have missed 4–12 surface rupture events in the exposures at the Sulphur Creek site.

We favor an explanation of distributed shear across the northern Sierra Nevada and Sierra Valley region. Deformation may be distributed across the MVFZ itself and/or accommodated by other regional faults. This type of slip distribution across the western portion of the NWL system would imply that surface rupture at the Sulphur Creek site accounts for only a fraction of the shear measured geodetically across the northern Sierra Nevada and Sierra Valley. In this regard, our findings are consistent with faulted continuum

models that incorporate a relatively low (0.5 ± 0.1 mm/yr) slip rate on the MVFZ and allow for distributed deformation in the region.

Because the MVFZ is a network of faults (Figure 2), it is possible that some amount of regional deformation after ~ 14 ka is not captured at the Sulphur Creek site. For example, on 27 October 2011, a M 4.7 earthquake with a strike-slip moment tensor occurred west of the main trace of the MVFZ, (http://comcat.cr.usgs.gov/earthquakes/eventpage/pde20111027063708570_16, accessed 12 December 2013). This moderate-magnitude earthquake could indicate the presence of uncharacterized but seismically active fault strands west of the main MVFZ. On balance, however, we consider it most likely that slip on the MVFZ not recorded at the Sulphur Creek site composes a small part of the overall strain accumulation budget because of the lack of geomorphic evidence of as yet uncharacterized faults with significant offset southwest of the mapped MVFZ, within the Sierra Nevada (Figure 2).

A more compelling explanation for the apparent discrepancy between the geodetic and geologic data on the MVFZ is that a system of as yet uncharacterized faults east of the MVFZ in Sierra Valley accommodates a large portion of the geodetically measured shear. *Gold et al.* [2013b] showed evidence for Quaternary slip on the Grizzly Valley fault (GVF), which is 18–20 km to the northeast (Figure 1). The GVF is not included as a boundary in the GPS block models, so the models may overpredict strain accumulation on the MVFZ; perhaps significant strain is also accumulating on the GVF. Figure 9 shows a transect of geodetic (data from *Hammond et al.* [2011], in Great Basin 09 reference frame) and seismicity data across the region (<http://www.quake.geo.berkeley.edu/anss/catalog-search.html>). The geodetic data show a trend of eastward decreasing velocity from the Sierra Nevada to the Diamond Mountains (Figure 9b) and no significant step in velocity across the MVFZ. In fact, the most distinct decrease in velocity appears to be located in Sierra Valley near the GVF. Furthermore, while seismicity is concentrated along the MVFZ, there are also prominent concentrations of seismicity both to the east and west of the MVFZ. East of the MVFZ, the seismicity corresponds to the Hot Springs fault (HSF) and GVF in Sierra Valley and in an area with no mapped faults near the Diamond Mountains in the eastern Sierra Valley (Figure 9c). Significant seismicity also occurs west of the MVFZ within the Sierra Nevada but does not correspond with a gradient in geodetic surface velocities. Finally, we note that the faulted continuum GPS models yield residual internal block deformation on the order of 1–2 mm/yr in Sierra Valley, which may correspond with structures like the GVF and HSF [*Field et al.*, 2013]. Collectively, these observations support the inference that deformation is distributed across a broader region than just the MVFZ.

There is increasing recognition that distributed strike-slip faulting plays an important role in accommodating shear in the Walker Lane [*Lifton et al.*, 2013]. The 2008 Reno-Mogul M 4.7 earthquake and swarm occurred approximately 50 km southeast of the Sulphur Creek site on a previously unrecognized strike-slip fault in the Reno basin [*Bell et al.*, 2012]. *Dong et al.* [2013] report a newly recognized strike-slip fault adjacent to the normal Wassuk Range front fault in the central Walker Lane. Studies such as these, as well as work documenting Quaternary strike-slip faulting on the Grizzly Valley fault system [*Gold et al.*, 2013b], imply that distributed strike-slip faulting may be a primary deformation mechanism in the Walker Lane and other broad zones of geodetically observed shear [e.g., *Walker et al.*, 2013]. These results suggest that intermediate solutions between rigid block models and continuum solutions may provide the most realistic representation of such regions [e.g., *Thatcher*, 2007].

Lastly, we cannot rule out the possibility that transient deformation might explain the high GPS block model strain accumulation rate across the MVFZ. In particular, the contemporary (decadal) strain rate may be unusually high and may have been significantly lower hundreds or thousands of years ago. This mechanism of transient strain has been invoked on the Garlock fault, although in an inverse sense [*Peltzer et al.*, 2001]. In another nearby example, a geologic record of Quaternary slip on the dextral Warm Springs Valley fault system [*Gold et al.*, 2013a], about 60 km to the northeast of the MVFZ (Figure 1), shows significant variability in late Quaternary slip rate, which was 2.5–3.8 mm/yr from 41.4–55.7 to 15.8 ka, but has slowed to <0.2 mm/yr from 15.8 ka to present. With these examples in mind, it is plausible that the Mohawk Valley fault could be currently experiencing an interseismic loading rate that exceeds its longer-term geologic slip rate. From a hazard assessment perspective, this high strain rate may indicate increased likelihood of fault rupture [*Amos et al.*, 2013; *Petersen et al.*, 2007], although because the strain gradient across Sierra Valley is broad (Figure 9) it is not clear which fault (MVFZ, GVF, or other) might fail.

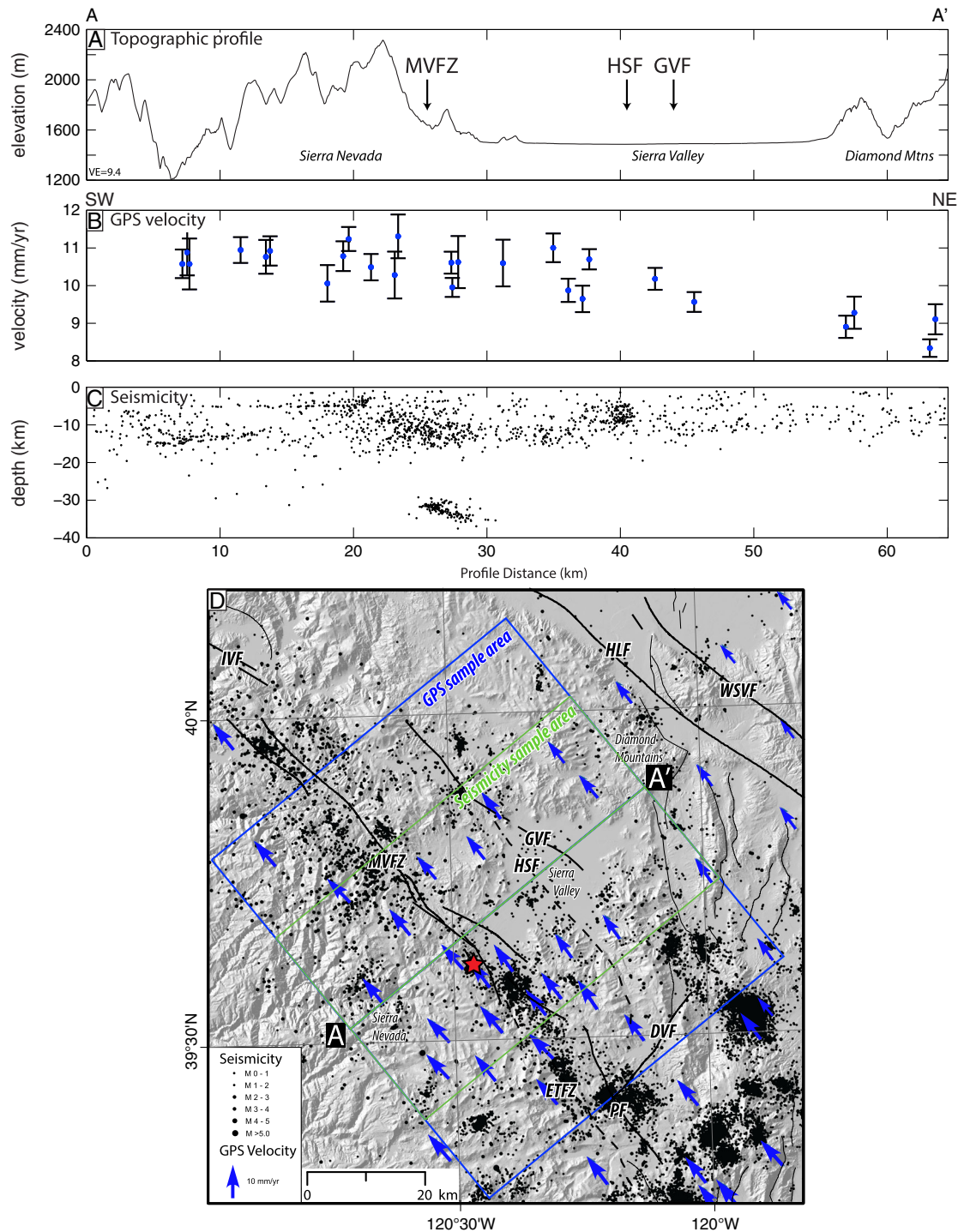


Figure 9. Northeast trending profile from the Sierra Nevada across Sierra Valley which crosses the mapped Mohawk Valley fault zone (MVFZ), Grizzly Valley fault (GVF), and Hot Springs fault (HSF). (a) Topography (National Elevation Data Set 10 m DEM). (b) Geodetic data from Hammond *et al.* [2011] in a Great Basin reference frame (GB09, uncorrected for postseismic relaxation), which show northwest-directed motion relative to the Great Basin to the east. The geodetic data show a gradual eastward decrease in velocities from the Sierra Nevada to the Diamond Mountains. (c) Historical seismicity from 1910 to 2013, M 0–5.3, showing a concentration of earthquakes along the mapped trace of MVFZ and other mapped faults in Sierra Valley (Advanced National Seismic System composite catalogue, <http://www.quake.geo.berkeley.edu/anss/catalog-search.html>, accessed 9 September 2013). The horizontal alignment of earthquakes at 5 km depth results from a default setting in the hypocentral location for earthquake with limited instrumental constraints. (d) Location map showing location of profile line A–A' and the corresponding swathes from which the geodetic (blue) and seismic data (green) were sampled. Red star indicates location of 27 October 2011, M 4.7 earthquake near the MVFZ.

8. Conclusions

Our paleoseismic investigation at the Sulphur Creek site documents evidence of four late Quaternary surface-rupturing earthquakes through the central portion of the MVFZ. Our results are compatible with a previous paleoseismic investigation to the south and are also consistent with the geomorphic expression of the fault trace, which is well defined by high-resolution lidar data. Our record of four latest Quaternary earthquakes and an average recurrence interval of 4 kyr are inconsistent with a ~ 3 mm/yr slip rate on the MVFZ inferred from geodetic block modeling, which would predict more than 10 m of slip per surface-rupturing earthquake or, alternatively, more frequent surface ruptures than observed at the Sulphur Creek site. The geologic and geodetic data might be reconciled if deformation is distributed across a broader region adjacent to the MVFZ in Sierra Valley such as the Grizzly Valley fault system and other uncharacterized structures, as implied by faulted continuum GPS models in the region. It is also possible that a high transient strain rate exceeds the average, long-term rate, such as observed along the nearby Warm Springs fault system. This study illustrates the importance of integrating geologic, geodetic, and other geophysical data sets to gain insight into deformation patterns across tectonically active regions such as the northern Walker Lane, where multiple faults individually accommodate modest (<1 to a few mm/yr) amounts of strain.

Acknowledgments

We thank Dan West and the Graeagle Land and Water Company for permission to conduct this study on private land. We also thank Tom Sawyer, Alan Ramelli, Lucille Piety, Joanna Redwine, Ralph Klinger, and Sarah Derouin for observations and critical field review of the trenches. Lee-Ann Bradley provided technical assistance drafting the trench logs. Scott Bennett and two anonymous reviewers provided thoughtful suggestions that significantly improved this manuscript. The U.S. Geological Survey Earthquake Hazards Program supported this work. Any use of trade, product, or firm names is for descriptive purposes only and does not imply endorsement by the U.S. Government.

References

- Ambraseys, N. (1971), Value of historical record of earthquakes, *Nature*, 232(5310), 375–379.
- Amos, C. B., S. J. Brownlee, D. H. Rood, G. B. Fisher, R. Bürgmann, P. R. Renne, and A. S. Jayko (2013), Chronology of tectonic, geomorphic, and volcanic interactions and the tempo of fault slip near Little Lake, California, *Geol. Soc. Am. Bull.*, doi:10.1130/b30803.1.
- Bell, J. W., F. Amelung, and C. D. Henry (2012), InSAR analysis of the 2008 Reno-Mogul earthquake swarm: Evidence for westward migration of Walker Lane style dextral faulting, *Geophys. Res. Lett.*, 39, L18306, doi:10.1029/2012GL052795.
- Bennett, R. A., A. M. Friedrich, and K. P. Furlong (2004), Codependent histories of the San Andreas and San Jacinto fault zones from inversion of fault displacement rates, *Geology*, 32(11), 961–964.
- Bird, P. (2009), Long-term fault slip rates, distributed deformation rates, and forecast of seismicity in the western United States from joint fitting of community geologic, geodetic, and stress direction data sets, *J. Geophys. Res.*, 114, B11403, doi:10.1029/2009JB006317.
- Bourne, S. J., T. Árnadóttir, J. Beavan, D. J. Darby, P. C. England, B. Parsons, R. I. Walcott, and P. R. Wood (1998), Crustal deformation of the Marlborough fault zone in the South Island of New Zealand: Geodetic constraints over the interval 1982–1994, *J. Geophys. Res.*, 103(B12), 30,147–30,165, doi:10.1029/98JB02228.
- Bronk Ramsey, C. (2008), Deposition models for chronological records, *Quat. Sci. Rev.*, 27(1–2), 42–60, doi:10.1016/j.quascirev.2007.01.019.
- Bronk Ramsey, C. (2009), Bayesian analysis of radiocarbon dates, *Radiocarbon*, 51(1), 337–360.
- California Department of Water Resources (1963), Areal geology of Sierra, Mohawk, Humboldt and Honey Lake Valleys ground water basins, in *Northeastern Counties Ground Water Investigation*, Bulletin, vol. 98, 224 pp., California Department of Water Resources, Sacramento, Calif.
- Cowan, H. A. (1990), Late Quaternary displacements on the Hope fault at Glynn Wye, North Canterbury, *N. Z. J. Geol. Geophys.*, 33(2), 285–293, doi:10.1080/00288306.1990.10425686.
- Cowan, H. A., and M. S. McGlone (1991), Late Holocene displacements and characteristic earthquakes on the Hope River segment of the Hope fault, New Zealand, *J. R. Soc. N.Z.*, 21(4), 373–384.
- Cowgill, E., R. D. Gold, X. Chen, X.-F. Wang, J. R. Arrowsmith, and J. R. Southon (2009), Low Quaternary slip rate reconciles geodetic and geologic rates along the Altyn Tagh fault, northwestern Tibet, *Geology*, 37(7), 647–650, doi:10.1130/G25623A.1.
- Dixon, T. H., S. Robaudo, J. Lee, and M. C. Reheis (1995), Constraints on present-day Basin and Range deformation from space geodesy, *Tectonics*, 14(4), 755–772, doi:10.1029/95TC00931.
- Dixon, T., M. Miller, F. Farina, H. Wang, and D. Johnson (2000), Present-day motion of the Sierra Nevada block and some tectonic implications for the Basin and Range province, North American Cordillera, *Tectonics*, 19(1), 1–24, doi:10.1029/1998TC001088.
- Dolan, J. F., and B. D. Haravitch (2014), How well do surface slip measurements track slip at depth in large strike-slip earthquakes? The importance of fault structural maturity in controlling on-fault slip versus off-fault surface deformation, *Earth Planet. Sci. Lett.*, 388, 38–47, doi:10.1016/j.epsl.2013.11.043.
- Dolan, J. F., D. D. Bowman, and C. G. Sammis (2007), Long-range and long-term fault interactions in southern California, *Geology*, 35(9), 855–858, doi:10.1130/g23789a.1.
- Dong, S., G. Ucarus, S. G. Wesnousky, J. Maloney, G. Kent, N. Driscoll, and R. Baskin (2013), Strike-slip faulting along the Wassuk Range of the northern Walker Lane, Nevada, *Geosphere*, doi:10.1130/ges00912.1.
- Duller, G. A. T. (2008), *Luminescence Dating: Guidelines on Using Luminescence Dating in Archaeology*, English Heritage, Swindon, U. K.
- Elliott, J. R., J. Biggs, B. Parsons, and T. J. Wright (2008), InSAR slip rate determination on the Altyn Tagh Fault, northern Tibet, in the presence of topographically correlated atmospheric delays, *Geophys. Res. Lett.*, 35, L12309, doi:10.1029/2008GL033659.
- Elliott, J. R., E. K. Nissen, P. C. England, J. A. Jackson, S. Lamb, Z. Li, M. Oehlert, and B. Parsons (2012), Slip in the 2010–2011 Canterbury earthquakes, New Zealand, *J. Geophys. Res.*, 117, B03401, doi:10.1029/2011JB008868.
- Faulds, J. E., and C. D. Henry (2008), Tectonic influences on the spatial and temporal evolution of the Walker Lane: An incipient transform fault along the evolving Pacific–North American plate boundary, in *Ores and Orogenesis: Circum-Pacific Tectonics, Geologic Evolution, and Ore Deposits: Arizona Geological Society Digest*, Arizona Geological Society Digest, vol. 22, edited by J. E. Spencer and S. R. Titley, pp. 437–470, Arizona Geological Survey, Tucson, Ariz.
- Faulds, J. E., C. D. Henry, and N. H. Hinz (2005), Kinematics of the northern Walker Lane: An incipient transform fault along the Pacific–North American plate boundary, *Geology*, 33(6), 505–508, doi:10.1130/G21274.1.
- Fialko, Y. (2006), Interseismic strain accumulation and the earthquake potential on the southern San Andreas fault system, *Nature*, 441(7096), 968–971, doi:10.1038/nature04797. [Available at http://www.nature.com/nature/journal/v441/n7096/supinfo/nature04797_S1.html.]

- Field, E. H., et al. (2013), The Uniform California Earthquake Rupture Forecast. Version 3 (UCERF3)—The Time-Independent Model, 97 pp., USGS Open-File Report 2013–1165.
- Friedrich, A. M., B. P. Wernicke, N. A. Niemi, R. A. Bennett, and J. L. Davis (2003), Comparison of geodetic and geologic data from the Wasatch region, Utah, and implications for the spectral character of Earth deformation at periods of 10 to 10 million years, *J. Geophys. Res.*, *108*(B4), 2199, doi:10.1029/2001JB000682.
- Ganev, P. N., J. F. Dolan, S. F. McGill, and K. L. Frankel (2012), Constancy of geologic slip rate along the central Garlock fault: Implications for strain accumulation and release in southern California, *Geophys. J. Int.*, *190*(2), 745–760, doi:10.1111/j.1365-246X.2012.05494.x.
- Gold, R. D., and E. Cowgill (2011), Deriving fault-slip histories to test for secular variation in slip, with examples from the Kunlun and Awatere faults, *Earth Planet. Sci. Lett.*, *301*(1–2), 52–64, doi:10.1016/j.epsl.2010.10.011.
- Gold, R. D., E. Cowgill, J. R. Arrowsmith, J. Gosse, X. Wang, and X. Chen (2009), Riser diachroneity, lateral erosion, and uncertainty in rates of strike-slip faulting: A case study from Tuzidun along the Altyn Tagh Fault, NW China, *J. Geophys. Res.*, *114*, B04401, doi:10.1029/2008JB005913.
- Gold, R. D., E. Cowgill, J. R. Arrowsmith, X. Chen, W. D. Sharp, K. M. Cooper, and X. F. Wang (2011), Faulted terrace risers place new constraints on the late Quaternary slip rate for the central Altyn Tagh Fault, northwest Tibet, *Geol. Soc. Am. Bull.*, *123*(5/6), 958–978, doi:10.1130/B30207.1.
- Gold, R., C. dePolo, R. Briggs, A. Crone, and J. Gosse (2013a), Late Quaternary slip-rate variations along the Warm Springs Valley fault system, northern Walker Lane, California-Nevada border, *Bull. Seismol. Soc. Am.*, *103*(1), 542–558, doi:10.1785/0120120020.
- Gold, R. D., W. J. Stephenson, J. K. Odum, R. W. Briggs, A. J. Crone, and S. J. Angster (2013b), Concealed Quaternary strike-slip fault resolved with airborne LiDAR and seismic reflection: The Grizzly Valley fault system, northern Walker Lane, California, *J. Geophys. Res. Solid Earth*, *118*, 3753–3766, doi:10.1002/jgrb.50238.
- Grose, T. L. T. (2000), Geologic map of the Blairsden 15' quadrangle, Plumas County, California, California Department of Conservation, Division of Mines and Geology, Sacramento, CA, Open-File report 2000–21, scale 1:62,500.
- Hammond, W. C., and W. Thatcher (2007), Crustal deformation across the Sierra Nevada, northern Walker Lane, Basin and Range transition, western United States measured with GPS, 2000–2004, *J. Geophys. Res.*, *112*, B05411, doi:10.1029/2006JB004625.
- Hammond, W. C., G. Blewitt, and C. Kreemer (2011), Block modeling of crustal deformation of the northern Walker Lane and Basin and Range from GPS velocities, *J. Geophys. Res.*, *116*, B04402, doi:10.1029/2010JB007817.
- Harkins, N., and E. Kirby (2008), Fluvial terrace riser degradation and determination of slip rates on strike-slip faults: An example from the Kunlun fault, China, *Geophys. Res. Lett.*, *35*, L05406, doi:10.1029/2007GL033073.
- Henry, C. D., J. E. Faulds, and C. M. dePolo (2007), Geometry and timing of strike-slip and normal faults in the northern Walker Lane, northwestern Nevada and northeastern California: Strain partitioning or sequential extensional and strike-slip deformation?, in *Exhumation Associated With Continental Strike-Slip Fault Systems*, Special Paper, vol. 434, edited by S. M. Roeske, J. C. Sample, and D. A. Foster, pp. 59–79, Geol. Soc. Am., Boulder, Colo.
- Herbert, J. W., M. L. Cooke, M. Oskin, and O. Difo (2013), How much can off-fault deformation contribute to the slip rate discrepancy within the eastern California shear zone?, *Geology*, doi:10.1130/g34738.1.
- Hubert-Ferrari, A., R. Armijo, G. King, B. Meyer, and A. Barka (2002), Morphology, displacement, and slip rates along the North Anatolian fault, Turkey, *J. Geophys. Res.*, *107*(B10), 2235, doi:10.1029/2001JB000393.
- Hunter, L. E., J. F. Howle, R. S. Rose, and G. W. Bawden (2011), LiDAR-assisted identification of an active fault near Truckee, California, *Bull. Seismol. Soc. Am.*, *101*(3), 1162–1181, doi:10.1785/0120090261.
- Kenner, S., and M. Simons (2005), Temporal clustering of major earthquakes along individual faults due to post-seismic reloading, *Geophys. J. Int.*, *160*(1), 179–194.
- Kirby, E., N. Harkins, E. Wang, X. Shi, C. Fan, and D. Burbank (2007), Slip rate gradients along the eastern Kunlun fault, *Tectonics*, *26*, TC2010, doi:10.1029/2006TC002033.
- Knuepfer, P. L. K. (1992), Temporal variations in latest Quaternary slip across the Australian-Pacific Plate boundary, northeastern South Island, New-Zealand, *Tectonics*, *11*(3), 449–464, doi:10.1029/91TC02890.
- Lifton, Z. M., A. V. Newman, K. L. Frankel, C. W. Johnson, and T. H. Dixon (2013), Insights into distributed plate rates across the Walker Lane from GPS geodesy, *Geophys. Res. Lett.*, *40*, 4620–4624, doi:10.1002/grl.50804.
- Marco, S., M. Stein, A. Agnon, and H. Ron (1996), Long-term earthquake clustering: A 50,000-year paleoseismic record in the Dead Sea Graben, *J. Geophys. Res.*, *101*(B3), 6179–6191, doi:10.1029/95JB01587.
- Matmon, A., D. P. Schwartz, P. J. Haeussler, R. Finkel, J. J. Lienkaemper, H. D. Stenner, and T. E. Dawson (2006), Denali fault slip rates and Holocene-late Pleistocene kinematics of central Alaska, *Geology*, *34*(8), 645–648, doi:10.1130/g22361.1.
- McClusky, S., et al. (2000), Global Positioning System constraints on plate kinematics and dynamics in the eastern Mediterranean and Caucasus, *J. Geophys. Res.*, *105*(B3), 5695–5719, doi:10.1029/1999JB900351.
- McClusky, S. C., S. C. Bjornstad, B. H. Hager, R. W. King, B. J. Meade, M. M. Miller, F. C. Monastero, and B. J. Souter (2001), Present day kinematics of the Eastern California Shear Zone from a geodetically constrained block model, *Geophys. Res. Lett.*, *28*(17), 3369–3372, doi:10.1029/2001GL013091.
- McGill, S., and K. Sieh (1993), Holocene slip rate of the central Garlock fault in southeastern Searles Valley, California, *J. Geophys. Res.*, *98*(B8), 14,217–14,231, doi:10.1029/93JB00442.
- Meade, B. J., and B. H. Hager (2005), Block models of crustal motion in southern California constrained by GPS measurements, *J. Geophys. Res.*, *110*, B03403, doi:10.1029/2004JB003209.
- Melody, A. D., B. B. Whitney, and C. G. Slack (2012), Late Pleistocene and Holocene faulting in the western Truckee Basin north of Truckee, California, *Bull. Seismol. Soc. Am.*, *102*(5), 2219–2224, doi:10.1785/0120110260.
- Nyst, M., and W. Thatcher (2004), New constraints on the active tectonic deformation of the Aegean, *J. Geophys. Res.*, *109*, B11406, doi:10.1029/2003JB002830.
- Olig, S., T. L. Sawyer, D. Wright, and F. Terra (2005), Preliminary seismic source characterization of faults near Stampede and Prosser Creek dams - Washoe Project and Boca Dam - Truckee storage project, in *Final Report*, URS, San Francisco, Calif.
- Oskin, M., L. Perg, E. Shelef, M. Strane, E. Gurney, B. Singer, and X. Zhang (2008), Elevated shear zone loading rate during an earthquake cluster in eastern California, *Geology*, *36*(6), 507–510, doi:10.1130/G24814A.1.
- Page, W. D., W. R. Lettis, and N. A. Abrahamson (1997), Characterization of seismic sources and estimated ground motions for Lake Almanor and Butt Valley dams, Plumas County, northeastern California, paper presented at Waterpower'97, ASCE.
- Peltzer, G., F. Crampé, S. Hensley, and P. Rosen (2001), Transient strain accumulation and fault interaction in the Eastern California shear zone, *Geology*, *29*(11), 975–978.
- Personius, S. F., A. J. Crone, M. N. Machette, S. A. Mahan, and D. J. Lidke (2009), Moderate rates of late Quaternary slip along the northwestern margin of the Basin and Range province, Surprise Valley fault, northeastern California, *J. Geophys. Res.*, *114*, B09405, doi:10.1029/2008JB006164.

- Petersen, M. D., T. Cao, K. W. Campbell, and A. D. Frankel (2007), Time-independent and time-dependent seismic hazard assessment for the State of California: Uniform California Earthquake Rupture Forecast Model 1.0, *Seismol. Res. Lett.*, *78*(1), 99–109, doi:10.1785/gssrl.78.1.99.
- Petersen, M., et al. (2008), Documentation for the 2008 update of the United States national seismic hazard maps, U.S. Geological Survey Open-File Report 2008–1128, 61 pp.
- Prescott, J. R., and J. T. Hutton (1994), Cosmic ray contributions to dose rates for luminescence and ESR dating: Large depths and long-term time variations, *Radiat. Meas.*, *23*(2–3), 497–500, doi:10.1016/1350-4487(94)90086-8.
- Redwine, J. L. (2013), *Quaternary history of Mohawk Valley, Northeastern California*, Univ. of Nevada, Reno.
- Reimer, P., et al. (2009), IntCal09 and Marine09 radiocarbon age calibration curves, 0–50,000 years cal BP, *Radiocarbon*, *51*(4), 1111–1150.
- Saucedo, G. J., and D. L. Wagner (1992), Geologic map of the Chico Quadrangle, *Map No. 7A*, California Department of Conservation, Division of Mines and Geology, scale 1:250,000.
- Sawyer, T. L. (1995), Fault number 25b, Mohawk Valley fault zone, Sierra Valley section, in *Quaternary Fault and Fold Database of the United States*, U.S. Geological Survey. [Available at <http://earthquakes.usgs.gov/hazards/qfaults/>], [accessed 14 March, 2014.]
- Sawyer, T. L., W. D. Page, and M. A. Hemphill-Haley (1993), Recurrent late Quaternary surface faulting along the southern Mohawk Valley fault zone, NE California, paper presented at Geological Society of America, Cordilleran Section, 89th annual meeting, Geol. Soc. Am., Reno, Nev.
- Sawyer, T. L., W. D. Page, and M. A. Hemphill-Haley (1995), Southern Mohawk Valley fault zone at the Calpine trench site, in *Quaternary Geology Along the Boundary Between Modoc Plateau, Southern Cascade Mountains, and Northern Sierra Nevada: Friends of the Pleistocene 1995 Pacific Cell Field Trip Guidebook*, edited by W. D. Page, Pacific Cell, San Francisco, Calif.
- Sawyer, T. L., R. W. Briggs, and A. R. Ramelli (2005), Late Quaternary activity of the southern Mohawk Valley fault zone, northeastern California, paper presented at SSA Annual Meeting, Lake Tahoe, Nev.
- Sawyer, T. L., R. W. Briggs, and A. R. Ramelli (2013), Paleoseismic investigation of the Mohawk Valley fault zone, Sierra County, northeastern California, 33 pp., NEHRP Final Technical Report.
- Schmalzle, G., T. Dixon, R. Malservisi, and R. Govers (2006), Strain accumulation across the Carrizo segment of the San Andreas Fault, California: Impact of laterally varying crustal properties, *J. Geophys. Res.*, *111*, B05403, doi:10.1029/2005JB003843.
- Shelef, E., and M. Oskin (2010), Deformation processes adjacent to active faults: Examples from eastern California, *J. Geophys. Res.*, *115*, B05308, doi:10.1029/2009JB006289.
- Sieh, K. E., and R. H. Jahns (1984), Holocene activity of the San Andreas fault at Wallace Creek, California, *Geol. Soc. Am. Bull.*, *95*, 883–896.
- Slack, C. G., T. Crampton, B. Gray, R. S. Rose, and L. E. Hunter (2011), LiDAR analysis and field mapping suggest tectonic linkage between the Truckee and Mohawk Valley fault zones, CA, paper presented at Association of Environmental and Engineering Geologists Annual Meeting, Anchorage, Alaska.
- Snyder, S., and J. Duval (2003), Design and construction of a gamma-ray spectrometer system for determining natural radioactive concentrations in geological samples at the U.S. Geological Survey in Reston, Virginia, *U.S. Geological Survey Open-File Report* 03–29.
- Thatcher, W. (2003), GPS constraints on the kinematics of continental deformation, *Int. Geol. Rev.*, *45*(3), 191–212.
- Thatcher, W. (2007), Microplate model for the present-day deformation of Tibet, *J. Geophys. Res.*, *112*, B05411, doi:10.1029/2005JB004244.
- Turner, H. W. (1897), *Downieville Folia*, Folios of the Geologic Atlas, vol. 37, pp. 1–8, U.S. Geological Survey, California.
- Turner, R., R. D. Koehler, R. W. Briggs, and S. G. Wesnousky (2008), Paleoseismic and slip-rate observations along the Honey Lake fault zone, northeastern California, U.S.A., *Bull. Seismol. Soc. Am.*, *98*(4), 1730–1736, doi:10.1785/0120070090.
- U.S. Geological Survey, Nevada Bureau of Mines and Geology, and California Geological Survey (2006), Quaternary fault and fold database for the United States. *USGS web site*: [Available at <http://earthquakes.usgs.gov/regional/qfaults/>].
- Van der Woerd, J., F. J. Ryerson, P. Tapponnier, Y. Gaudemer, R. Finkel, A. S. Meriaux, M. Caffee, G. Zhao, and Q. He (1998), Holocene left-slip rate determined by cosmogenic surface dating on the Xidatan segment of the Kunlun fault (Qinghai, China), *Geology*, *26*(8), 695–698.
- Van der Woerd, J., P. Tapponnier, F. J. Ryerson, A.-S. Meriaux, B. Meyer, Y. Gaudemer, R. C. Finkel, M. W. Caffee, G. Zhao, and Z. Xu (2002), Uniform postglacial slip-rate along the central 600 km of the Kunlun fault (Tibet), from ²⁶Al, ¹⁰Be and ¹⁴C dating of riser offsets, and climatic origin of the regional morphology, *Geophys. J. Int.*, *148*, 356–388.
- Walker, R. T., et al. (2013), The 2010–2011 South Rigan (Baluchestan) earthquake sequence and its implications for distributed deformation and earthquake hazard in southeast Iran, *Geophys. J. Int.*, doi:10.1093/gji/ggs109.
- Wallace, K., G. Yin, and R. Bilham (2004), Inescapable slow slip on the Altyn Tagh fault, *Geophys. Res. Lett.*, *31*, L09613, doi:10.1029/2004GL019724.
- Wells, D. L., and K. J. Coppersmith (1994), New empirical relationships among magnitude, rupture length, rupture width, rupture area, and surface displacement, *Bull. Seismol. Soc. Am.*, *84*(4), 974–1002.
- Wills, C. J., and G. Borchardt (1993), Holocene slip rate and earthquake recurrence on the Honey Lake fault zone, northeastern California, *Geology*, *21*(9), 853–856.
- Zhang, P.-Z., et al. (2004), Continuous deformation of the Tibetan Plateau from global positioning system data, *Geology*, *32*(9), 809–812.